Mechatronics 109 (2025) 103334

Contents lists available at ScienceDirect

Mechatronics

journal homepage: www.elsevier.com/locate/mechatronics

A visco-elastic actuator with linear gas spring and variable damping

Florian C. Loeffl [a,*], Fabian Beck [a], Jinoh Lee [a,b], MinJun Kim [c], Manuel Keppler [a]

[a] Institute for Robotics and Mechatronics, German Aerospace Center, Oberpfaffenhofen, Germany
[b] Department of Mechanical Engineering, Korea Advanced Institute of Science and Technology (KAIST), Daejeon, South Korea
[c] Intelligent Robotics Lab, Korea Advanced Institute of Science and Technology (KAIST), Daejeon, South Korea

ARTICLE INFO

Keywords:
Variable impedance actuation
Damping
Robots
Actuators
Cable driven robots
Human–robot interaction
Legged robots
Series elastic actuation
Design
Springs

ABSTRACT

Series elastic actuators (SEAs) enhance safety and robustness in robotic joints but sacrifice torque and motion bandwidth compared to rigid actuators. Variable viscoelastic actuators (VVEAs) overcome these limitations by integrating an adjustable damping element with a spring, balancing open-loop torque bandwidth with impact safety and robustness. However, most existing VVEA designs rely on mechanical springs that add significant weight. We introduce a lightweight VVEA based on a pneumatic spring design. This actuator achieves linear, offline-adjustable stiffness using antagonistic gas chambers and provides online-adjustable damping via a hydraulic throttle valve. In our design, the increasing force of one chamber is moderated by the decreasing force of the other, resulting in a measured maximal deviation of 12% from the linear model. Additionally, an elastic silicone cast bladder replaces the conventional ring-shaped piston, significantly reducing breakaway force. To evaluate its benefits over standard actuators, we applied optimal control to periodic rest-to-rest motions typical of pick-and-place tasks. Based on mean tracking error, the VVEA outperforms SEAs in 29.1% of trials and rigid actuators in 89.2% of trials. Although increasing damping improves performance, it compromises safety; our optimization study demonstrates the potential of an online variable damping setpoint to balance these trade-offs. These results suggest that VVEAs hold great promise for applications requiring rapid maneuvers and enhanced impact safety and robustness.

1. Introduction

Since the introduction of series elastic actuation (SEA) [1], such actuators have been investigated due to their impact robustness and prospect on energy efficient actuation in resonant motions. To exploit resonance, the plants' intrinsic frequencies need to match the intended motion frequencies, which leads to low physical stiffness elements in the actuation drivetrain. Those elements introduce torque bandwidth limitations on task frequency. Force transmission elements such as clutches or dampers placed in parallel to the elastic element increase the frequency bandwidth [2]. While clutches exhibit a clutch force dependent transmission behavior, fluid dampers usually generate speed dependent forces. This means for raising motion frequencies and thus higher displacement speeds, the influence of damping forces increases. Within the drivetrain we interpret this as combining a low pass element, the spring, with a high pass element, the damper. In theory, the variation of the damping parallel to the series elastic element allows the online adaption of the actuators' dynamics from pure series elastic behavior featuring zero damping, to a rigid drivetrain at which the damping approaches infinity. In contrast to varying the stiffness in a variable stiffness actuator, the variation of the damping coefficient does not have any immediate effect on the energy of the system. While a change of the damping coefficient does not inject or remove energy at the system, the adjustment of the stiffness effects the energy distribution by changing the amount of energy in the system or by modifying the equilibrium points of the system.

The benefits of variable physical damping in compliant actuators has inspired a variety of designs (see Table 1). According to Monteleone et al. [10], these designs can be classified based on three criteria: passive versus active control, the operating principle, and the topological position of the damping element. For example, the biped robot Blue [3] achieves variable damping using electromagnetic actuators. Although Blue also incorporates variable stiffness, its separation of stiffness and damping into separate mechanism adds integration complexity. In contrast, the CompAct actuator [6] features a variable damper built from piezoelectric stacks that generate braking torque when activated, yet this system requires active control to regulate and estimate viscous damping at the joint. Catalano et al. [4] introduced a damping module based on meatus technology, where damping forces arise from the relative motion between the driveshaft and its housing. However, this topology does not benefit from the high-frequency bandwidth offered by a damper arranged in parallel with a series spring. Similarly, the

* Correspondence to: Münchener strasse 20, 83234, Wessling, Germany.
E-mail address: florian.loeffl@dlr.de (F.C. Loeffl).

https://doi.org/10.1016/j.mechatronics.2025.103334
Received 21 December 2024; Received in revised form 14 April 2025; Accepted 22 April 2025
Available online 14 May 2025

Table 1
Variable damping modules and actuators.

	Type	Spring			Damper	
		Topology	Characteristic	Variable	Characteristic	Variable
Enoch et al. [3]	Mechanical	SEAwEPD	Nonlinear	Online	Linear	Online
Catalano et al. [4]	Mechanical	SEAwEPD	Linear	Online	Linear	Online
Accoto et al. [5]	Mechanical	SEDA	Nonlinear	No	Linear	Offline
Laffranchi et al. [6]	Mechanical	SEDA	Linear	No	Linear[a]	Online
Zhi et al. [7]	Mechanical	SEDA	N.a.	No	Nonlinear	Online
Yin et al. [8]	Pneumatic	SEDA	Nonlinear	Online[b]	Nonlinear	Online[b]
Yuan et al. [9]	Mechanical	SEDA	Linear	No	Nonlinear	Online
Our	Pneumatic	SEDA	Linear	Offline	Linear	Online

[a] Achieving linear behavior requires active control.
[b] Characteristics adjustable in discrete steps.

viscoelastic joint pVEJ [5] features variable fluid-based damping but does not allow online adjustment of the damping setting; furthermore, varying the spring stiffness requires mechanical modifications. Designs based on rotational hydraulic cylinders, such as those by Zhi et al. [7] and Yuan et al. [9], provide online adaptability of the damping setting but still rely on mechanical springs. Yin et al. [8] proposed a variable suspension element with similar mechanisms to our design; however, it is limited by its discrete selection of damping and spring characteristics and the gas spring lacks a mechanism to achieve a linear behavior. Magnetorheological (MR) fluids, which adjust shear strength under a magnetic field, offer an attractive alternative. Although MR fluids are widely applied in vibration control, brakes, clutches, and dynamometers [11], their potential in robotic actuators remains largely untapped. Notably, all these VVEA designs — except the one proposed by Yin et al. [8] — rely on mechanical springs that add significant weight. In contrast, pneumatic spring designs like Yin's offer considerable weight savings. However, achieving linear spring characteristics — which enable the use of linear control and analysis techniques — remains a significant challenge with pneumatic designs.

To bridge this gap, we introduce a lightweight spring–damper unit for compliant actuation that features continuously (offline) adjustable stiffness via a quasi-linear gas spring and an online adaptable fluid damper. The complete unit weighs 638 g, provides 40 mm of travel, and offers stiffness adjustments from 2.3 to 233 N/mm. For comparison, a steel spring with equivalent travel and stiffness (excluding additional mechanisms) weighs 395 g. Based on a pull-spring design, our unit is especially suited for tendon-driven systems. We further benchmark our variable viscoelastic actuator against standard series elastic actuators (SEAs) and rigid joint actuators in an optimal control study. For periodic rest-to-rest motions typical of pick-and-place tasks, the VVEA outperforms SEAs in 29.1% of trials and rigid actuators in 89.2% of trials, based on mean tracking error. Although increasing physical damping increases control bandwidth, it also compromises safety [12]. Therefore, a damping setpoint policy should aim for the lowest possible damping to ensure safety. To assess the safety potential of an online variable damping setpoint, we compared it to actuators with constant damping in an optimal torque control study. Our results shows that the VVEA approaches closely the step response performance of highly damped actuators while operating at significantly lower peak and average damping levels.

Overall, this work advances the state of the art by providing:

- The design of a lightweight versatile actuator component with an elastic silicone cast bladder reducing friction.
- A design guide for a linear, offline adjustable pneumatic spring design based on antagonistic gas chambers.
- An optimization study evaluating the performance gain of such actuators for periodic rest to rest motions.

2. Working principle

The proposed spring–damper system is designed as a pull spring, to make it suitable for tendon driven robots. Referring to Fig. 1 a pneumatic spring system (dark- and light-blue), with antagonistic working gas chambers ② and ③ acting on a working piston ① provides an adjustable spring characteristics. This is combined with a hydraulic system (green), with an adjustable throttle fluid damper ④ and an integrated blow off valve ⑤ to avoid overloads on high speed displacements.

Table 2
Technical data of the spring–damper unit.

Size	132.5 mm × 59.5 mm
Weight	638 g
Travel	40 mm
Damping range	0.4 N s mm^{-1}–1025 N s mm^{-1}
Stiffness range	2.3 N mm^{-1}–233 N mm^{-1}
Coulomb friction	125 N

Remark 1. The integrated working principle imposes an retraction speed limitation, as the damping forces counteract the retracting spring forces when unloading. This primarily becomes noticeable on high damping values and low spring pretension.

2.1. Damping mechanism

We choose an orifice valve to adjust the flow area of the damping system. With this valve type the damping can be adjusted fast, reliably and with low forces. A Blue Bird BMS-390DMH servo drive is tuning the damping from closed to full open within less than 0.1 s. A pressure relief gate bypassing the throttle avoids excessive forces generated by high piston speeds. Pressure losses in the turbulent flow of viscous fluids provide a reliable speed dependent energy dissipation mechanism, that can be rendered by simple models.

2.2. Spring mechanism

As proposed in Section 3.2 we utilize a system of two gas springs opposing each other to obtain a linear spring characteristics. Nonlinear progression of chamber ② pressures, that get transferred to the working piston ① through the hydraulic fluid, is mildered by the degression of chamber ③. Well chosen volumes of these chambers can result in nearly linear spring characteristics, as detailed in Section 3.2.

3. Prototype design

We built a prototype to evaluate the proposed VVEA design. This section, discusses the design of hydraulic damper, the gas spring and the silicon bladder that separates the fluid ② and gas ③ in the out chamber. A cross section of the proposed design is shown in Fig. 2. Additionally, the technical specifications are summarized in Table 2.

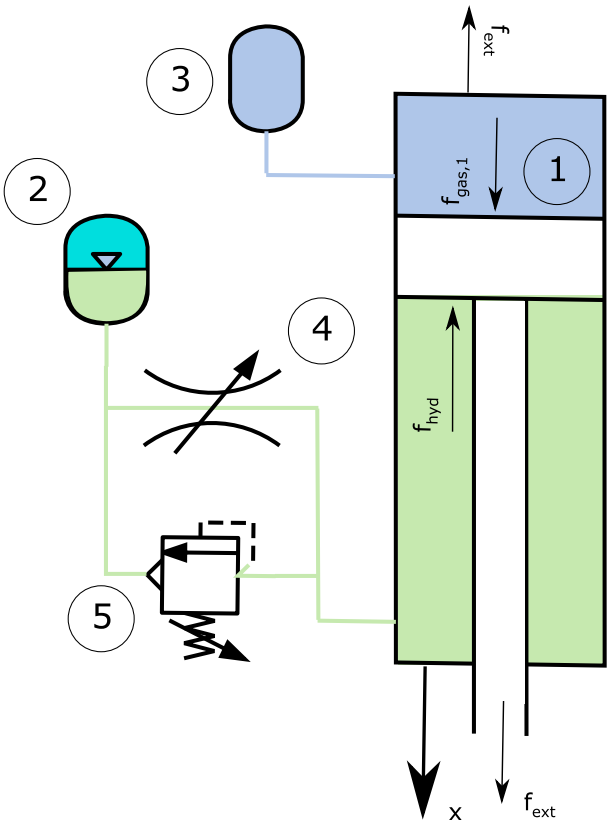

Fig. 1. Schematic of the VVEA. The blue components represent the pneumatic spring system, including the working piston (1), positive air chamber (2), and negative air chamber (3). The green components depict the hydraulic system, comprising a fluid damper with an adjustable throttle (4) and a blow-off valve (5).

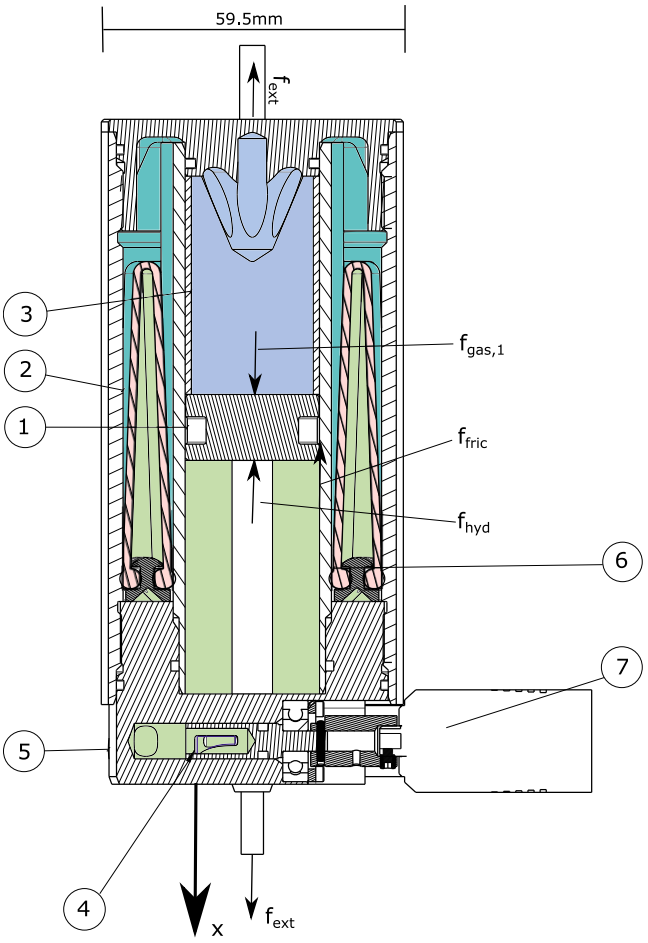

Fig. 2. Section through the highly integrated concentric layout of the spring–damper unit with the main components: (1) working piston; (2) positive gas chamber (red); (3) negative gas chamber (blue); (6) hydraulic fluid bladder and hydraulic system (green); (4) adjustable damping valve; (7) adjustment servo motor; (5) pressure relief valve (not drawn).

3.1. Hydraulic damper design

The hydraulic system is mainly contained in the bottom part of the system. Fluid channels, not depicted in the section, connect the inner chamber via the throttle valve (4) to the outer chamber. From the motion of the piston (1) displaced fluid can flow through the valve (4) and fill the bladder (6). The gas in the outer chamber (2) is compressed and raises the pressure on the fluid and thus the force on the piston (1).

We choose a rotary valve with symmetric ports for the throttle, to avoid pressure dependent operating forces. A servo motor (7) turning the cylindrical valve (4) allows to change the aperture of the flow channel. The channel window (rectangular) and the shape of the valves' opening are clearly visible in Fig. 2. Pressure losses at the throttle add to the gas spring forces and generate the damping action.

To avoid damage by excessive damping forces a pressure relief gate (5) is bypassing the throttle. We use a preloaded spring-ball type for this.

3.2. Gas spring design

Since the hydraulic system needs to be sealed anyway, it was convenient to choose a compressible gas spring as the energy storage in this device. A gas spring is relatively light weight, comes with easy tuning, but suffers on a non-linear force–displacement characteristic $f(x) = 1/x$, when modeling the spring as isotherm compression of an ideal gas [13].

In many use cases a linear characteristic is requested. We obtain this by a structure of two gas springs opposing each other. The decreasing grade of one spring moderates the increasing of the other. In this set-up the force–displacement characteristic is a function of the variable displacement and the parameters, piston area and dead volumes. In our design we could obtain a linearity deviation of the mathematical model less than 2%.

3.2.1. Antagonistic gas spring design

We calculate the generated external forces f_{ext} of our system by considering a mechanical equilibrium for the inner piston

$$f_{ext} = f_{hyd} + f_{fri} - f_{gas,1}, \tag{1}$$

with f_{hyd} being the hydraulic forces pushing the piston inside the housing, $f_{gas,1}$ the forces of the gas in the first (inner) chamber (see (1) in Fig. 1) pushing the piston outside and f_{fri} the sealing friction forces. The hydraulic forces can be calculated as

$$f_{hyd} = f_{gas,2} - f_{flow}, \tag{2}$$

with $f_{gas,2}$ the forces of the gas in the second (outer) chamber (see (2) in Fig. 1) and f_{flow} the flow resistance in the throttle valve.

To obtain the force f_{gas} generated by the two gas spring components, we combine (1) and (2), which yield

$$f_{ext} = \underbrace{f_{gas,2} - f_{gas,1}}_{f_{gas}} + f_{fri} - f_{flow}. \tag{3}$$

To obtain the individual forces of each chamber we assume an isothermal and reversible process such that we can apply the ideal gas law,

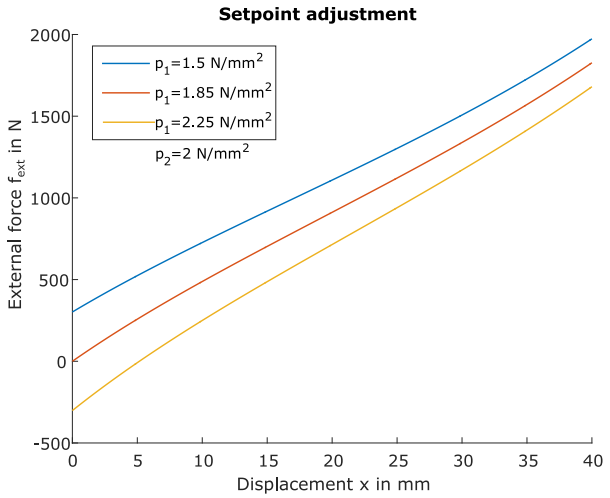

Fig. 3. Force over displacement for different pressure setpoints: Changing p_1/p_2 changes zero crossing of force–displacement curve (setpoint).

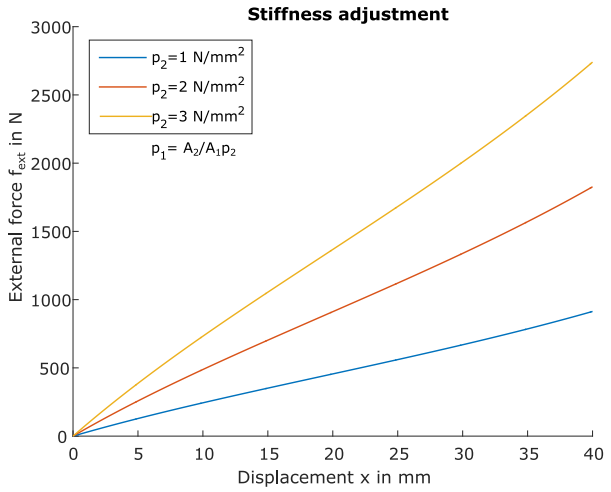

Fig. 4. Force over displacement for different pressure presets: Increasing p_2 for constant p_1/p_2 ratio increases stiffness.

which yield

$$f_{gas,i}(y) = A_i\ p_i\ \frac{V_i}{V_i - A_i y} \text{ for } i \in \{1,2\}, \tag{4}$$

where y is the displacement of the piston towards compression and A_i denotes the active surface of the piston in chamber i. Moreover, p_i is the initial pressure and V_i denotes the initial chamber volume both at $y = 0$ for component i.

Combining (4) in (3) we obtain

$$\begin{aligned} f_{gas}(x) &= f_{gas,2}(x) - f_{gas,1}(-x) \\ &= A_2 p_2\ \frac{V_2}{V_2 - A_2 x} - A_1\ p_1\ \frac{V_1}{V_1 + A_1 x}, \end{aligned} \tag{5}$$

where x denotes the displacement of the common piston as defined in Fig. 2.

The proposed design allows to preset p_1, p_2 and V_2, providing the possibility to adjust spring stiffness, spring progression and setpoint of the spring.

3.2.2. Setpoint adjustment

The setpoint of a spring is the displacement, where the spring forces are zero. By setting (5) to zero and solving for p_1 we obtain for a non-zero initial displacement x_0

$$p_1 = \frac{A_2}{A_1}\frac{V_2}{V_2 - A_2 x_0}\frac{V_1 + A_1 x_0}{V_1} p_2, \tag{6}$$

and for x_0 equals zero

$$p_1 = \frac{A_2}{A_1} p_2. \tag{7}$$

Remark 2. To set setpoint and stiffness characteristics the chamber pressure of both chambers need to be set while taking the actual piston displacement into account.

In Fig. 3 force–displacement plots for three different setpoints are drawn. The zero force crossing varies in a range of ±5 mm around zero. This means also pre-tensioned springs can be set.

3.2.3. Spring stiffness adjustment

Adjustment of the spring stiffness is possible, as it is linearly dependent on the pressure preset p_2 and p_1. This can be shown by analyzing (5). The piston areas A_i are constant, and the fraction of the two summands for f_{gas} only dependent on geometric values. This means p_i is linearly scaling the force curve.

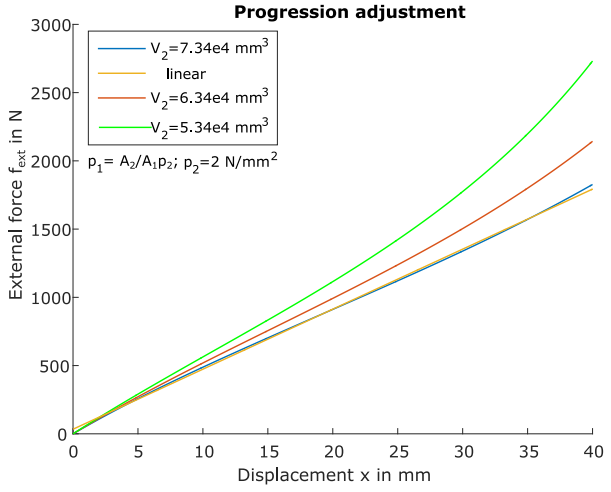

Fig. 5. Force over displacement for different volumes of V_2: Smaller values of V_2 result in a progressive force–displacement characteristics. Comparing the linear fit with the setting $V_2 = 7.34 \times 10^4$ mm^3 shows a linearity deviation of 1.86%.

The plots in Fig. 4 depict the spring characteristics for different pressure settings. All curves share the same near linear shape but differ in their mean slope.

3.2.4. Spring progression adjustment

Changing the total volume of hydraulic fluid filled into the system, directly affects the chamber volume V_2, since V_1 is fixed by design. Increasing the volume of incompressible fluid reduces the volume left for compressible gas in the second chamber. A smaller gas volume will effect in a more progressive spring characteristics.

Fig. 5 shows the force over displacement plots for different settings of V_2. We use the setting $V_2 = 7.34 \times 10^4$ mm^3 to generate a nearly linear spring characteristic. We obtain an error of 33.98 N at a maximum force of 1827 N with this setting. This means the maximal force deviation error over the displacement range normalized by the maximal force value is 1.86%.

Based on a chosen inner piston diameter of 30 mm and the fact, that the needed travel of 40 mm and the length the volume for the inner chamber V_1 needs add up to the total length of the outer chamber, only the overall outer diameter had to be hand optimized to obtain good linearity. We found $V_1 = 1.22 \times 10^5$ mm^3 with the resulting total

Fig. 6. Photo of the elastic silicone cast bladder to separate hydraulics from pneumatics.

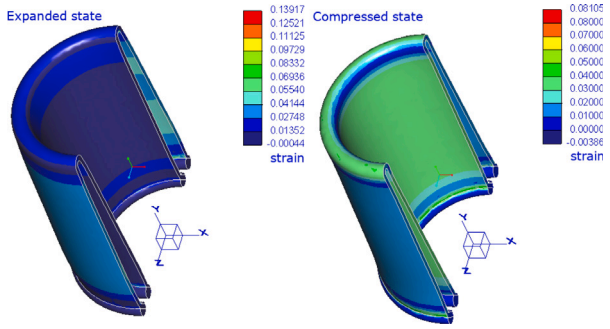

Fig. 7. FEM simulation of the bladder with the piston at the outer (left) and inner (right) positions, corresponding to fully expanded and compressed states, respectively. The bladder pressure varies from 0.03 MPa (expanded) to −0.03 MPa (compressed). Colors indicate the material strain under these inner pressure conditions.

housing length of 132 mm and $V_2 = 7.34{\times}10^4$ mm^3 as a good compromise for size, working pressures, and linearity as Fig. 5 shows.

3.3. Bladder design: Separating fluid and gas

The bladder (6) is one main component of the system reducing friction losses. It replaces a ring shaped piston separating the fluid from the gas in the outer chamber. Tiny elastic deformations of the bladder take place of this pistons motions, that where subject to friction. Compared to the identification results of the piston the bladder design has 21.2% less Coulomb friction.

We manufacture the bladder itself by silicone casting in a 3D printed form as shown in Fig. 6. A support ring is also part of the bladder design. It is the dark part at the lower end of the bladder in Fig. 2. Also 3D printed, it is generating joining pressure to seal the bladder to the shell of the inner and outer tube. The support ring has channels allowing the damping fluid to get in and out of the bladder.

To analyze the behavior of the bladder during operation, an finite element analysis has been performed evaluating the occurring strains caused by the displaced fluid volume. Fig. 7 shows the displaced result of the analysis with ±0.03 MPa pressure load, where the colors encode the occurring strain in the material. The volume difference of the two load cases corresponds to the volume change of a full stroke of the inner piston. Maximal strains of approx 14% respective 8% are considered uncritical compared to a breaking strain of 100%–600% usually present in silicon materials. The differential pressure of 0.03 MPa applied to obtain the displacement is considered to be negligible compared to the operating pressure of 1 MPa to 4 MPa. As the differential pressures caused by the deformation of the bladder are the only ones the sealing faces are object to, no excessive leakage is expected.

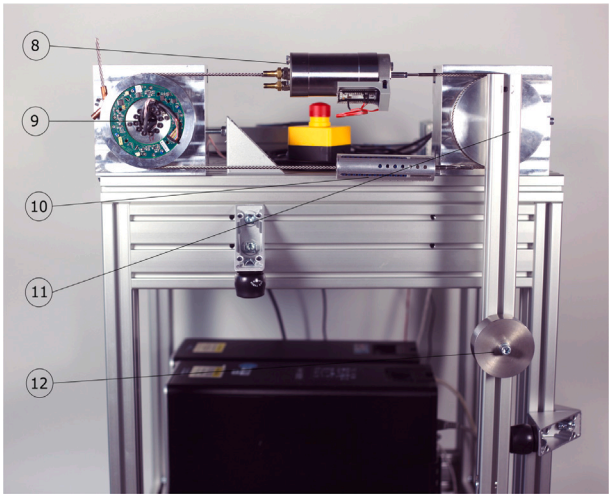

Fig. 8. Series elastic actuator setup.

3.4. Complete actuator

Fig. 8 shows the setup of our actuator setup. As also implemented in the DLR C-Runner system (see [14]), we choose a tendon pulley drive with two pre-loaded elastic elements (8), (10) to transmit torques from the motor-gearbox unit to the link. A DLR-LWR joint (see [15]) represents the motor-gearbox unit (9) in this setup. A simple lever arm (11) with a mass (12) acts as a link load.

Assuming no external loads, we model the systems dynamics as (see for example [7])

$$B\ddot{\theta} + D(\dot{\theta} - \dot{q}) + K(\theta - q) + C_f = \tau_m, \tag{8}$$

$$M\ddot{q} - D(\dot{\theta} - \dot{q}) - K(\theta - q) - C_f = 0, \tag{9}$$

where q and θ is the link and motor position, respectively.

Moreover, K denotes the series elastic stiffness and D is the variable damping coefficient. The motor inertia is $B = 0.598\,\mathrm{kg\,m^{-2}}$ and link inertia is given by $M = 1\,\mathrm{kg\,m^{-2}}$. C_f denotes friction forces not further modeled. The torque acting at the link is

$$\tau = D(\dot{\theta} - \dot{q}) + K(\theta - q) + C_f.$$

To take the dynamics of the valve adjuster motor into account the dynamics of D is modeled as

$$\dot{D} = u_d, \tag{10}$$

where the control input is given by u_d. Moreover, the dynamics (10) is subject to the constraint

$$D_{min} < D(t) < D_{max} \tag{11}$$

and the initial condition $D(0)$ is chosen to be D_{min}. Furthermore, the valve adjuster motor dynamics is subject to actuator saturation effects, which will be modeled by

$$\|u_d\| \leq 1 \times 10^4\,\mathrm{N\,m\,rad^{-1}\,s^{-2}}. \tag{12}$$

The motor torque τ_m is the second input to the actuator system. It is subject to the saturation:

$$\|\tau_m\| \leq 100\,\mathrm{N\,m}. \tag{13}$$

4. Identification: Spring-damper element

This section focuses on the identification of the main new component in the VVEA setup, the spring–damper element. To identify the physical parameters, we performed and evaluated over 135 experiments. By parameter optimization a simple model was fit to the data, identifying the stiffness per pressure value g, the Coulomb friction value C and the viscose damping values D_i for each valve setting.

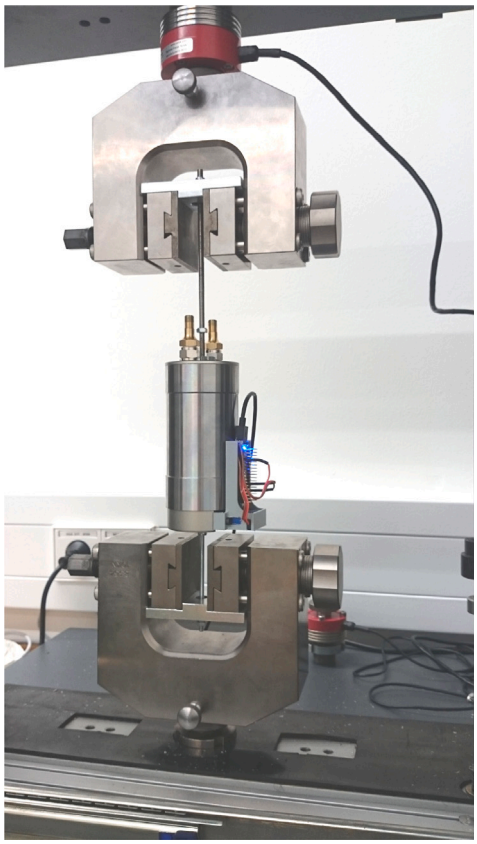

Fig. 9. Experimental setup for identification.

4.1. Experimental setup

We used an industrial grade tension testing machine from the manufacturer Zwick for our experiments. Fig. 9 shows the spring–damper unit mounted in the testing machine. Loading experiments for each combination of three pressure presets $p_2 \subset \{1\,\text{MPa}, 2\,\text{MPa}, 4\,\text{MPa}\}$ and nine valve positions $\gamma \subset \{50°, 80°, 100°, 104°, 106°, 108°, 109°, 110°, 120°\}$ where performed. For each experiment we displaced the unit 40 mm at constant speed. To allow a proper identification of the damping value, the displacement speed was varied for $\dot{x} \in \{0.1\,\text{mm s}^{-1}, 1\,\text{mm s}^{-1}, 4\,\text{mm s}^{-1}, 8\,\text{mm s}^{-1}, 12\,\text{mm s}^{-1}\}$.

4.2. Identification method

Though orifice type dampers typically generate speed dependent forces, we tried to fit a simple linear spring–damper–friction model aligned to (9) and (8), to characterize the system's dynamic behavior. It proposes a linear dependency g from the pressure preset, a linear damping value L and a simple Coulomb friction model. We model the estimated external force $\hat{f}_{ext}$ with:

$$\hat{f}_{ext} = g\ p_2\ x + L\ \dot{x} + C\ \text{sign}(\dot{x}). \tag{14}$$

Deploying Matlab's *fmincon* function we solve the minimization problem:

$$\min_{g,B,L(\gamma)} \left(\sum_{i=1}^{n} \left(f_{ext}(i) - \hat{f}_{ext}(x(i), \dot{x}(i)) \right)^2 \right), \tag{15}$$

determining the model parameter g, C and $L(\gamma)$.

Table 3
Identified model parameters.

Parameter	Unit	Value
g	$\text{N mm}^{-1}\,\text{MPa}^{-1}$	23.31
B	N	125.5
L(50)	N s mm^{-1}	0.4
L(80)	N s mm^{-1}	0.5
L(100)	N s mm^{-1}	7.1
L(104)	N s mm^{-1}	15.1
L(106)	N s mm^{-1}	25.3
L(108)	N s mm^{-1}	40.6
L(109)	N s mm^{-1}	52.7
L(110)	N s mm^{-1}	85.2
L(120)	N s mm^{-1}	1024.7

4.3. Results

4.3.1. Identified parameters

Table 3 is summing up the identified model parameters. Note: The damping value $L(120)$ contained in the table marks the damping for a fully closed valve. This setting results in a nearly blocked system, behaving like a stiff actuator in practical use.

A force estimation calculated with the model in Eq. (15) using the parameters in Table 3 can reproduce the measured forces with an error in the range of −9.5% to 12.0% of the nominal force. Fig. 10 compares the measurements F of the identification experiments with the estimated forces $F_{model} = \hat{f}_{ext}(x, \dot{x}, g, C, L)$ under 5 displacement speeds and 9 damping valve positions.

4.3.2. Spring characteristic

Fig. 11 shows a characteristic force–displacement plot for an experiment at low speed of $\dot{x} = 0.1\,\text{mm s}^{-1}$ and medium pressure preset of $p_2 = 2\,\text{MPa}$. The plot shows clear stiction at the start and the turning point of the motion. Though the absolute error of 188.6 N stays below 9.3% of the maximum force.

5. Actuator comparison: Rest-to-rest motions

Utilizing the damping value set-point as an control input to the system can reduce the accumulated tracking error for a periodic rest-to-rest motions. With the additional input u_d the VVEA forms an MISO system. The selection of the control inputs is not unique for a link-side position trajectory, which solely depends on the acting link side torque τ. Thus, different control strategies may utilize the additional damping input in different ways. In order to analyze the system performance independent of the actual controller implementation, in the following an optimal control problem is formulated and the performance is evaluated in a numerical simulation.

5.0.1. Problem definition

In the following we consider an alternating piece-wise constant link position reference q_{des} with amplitude A and period T given by

$$q_{des}(t) = \begin{cases} 0 & \text{for } 0 \le t \bmod T < \frac{1}{2}T \\ A & \text{for } \frac{1}{2}T \le t \bmod T < T. \end{cases}$$

With this, we define the optimization problem to minimize the $\mathcal{L}_2$ norm of the tracking error $q - q_{\text{des}}$, i.e.,

$$\min_{\tau_m, u_d} \int_0^{t_e} (q - q_{\text{des}})^2 dt, \tag{16}$$

where the $\mathcal{L}_2$ norm is evaluated over a finite time horizon $t_e = 2T$. The minimization problem is subject to the system dynamic Eqs. (8), (9) and (10) as well as the constraints on motor torque and damper variability given by (13), (11) and (12). For faster simulations we simplified our model by setting the friction $C_f = 0$.

The nonlinear optimization problem was solved using a direct collocation method implemented in the CasADi framework [16]. The

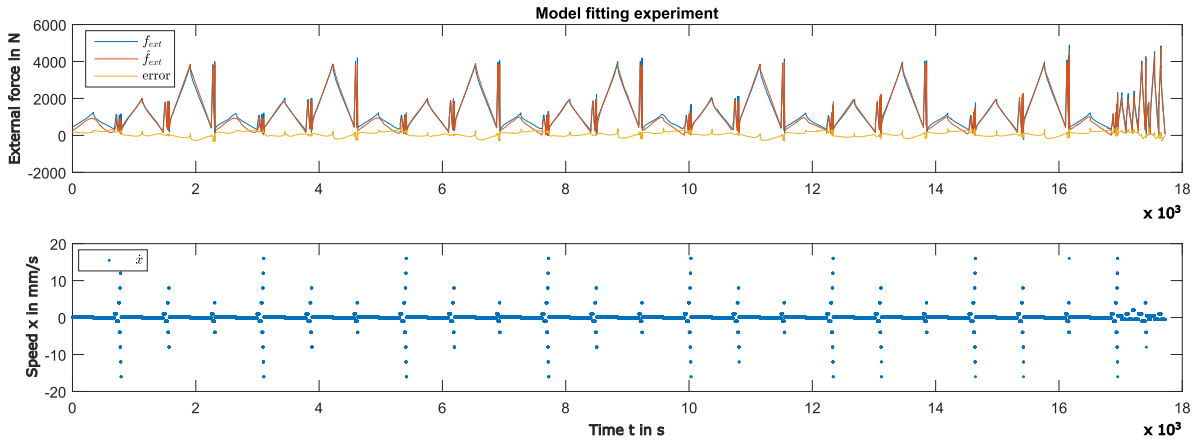

Fig. 10. Identification experiments: Measurement, model prediction and error at different displacement speeds, pressure presets and damper valve positions.

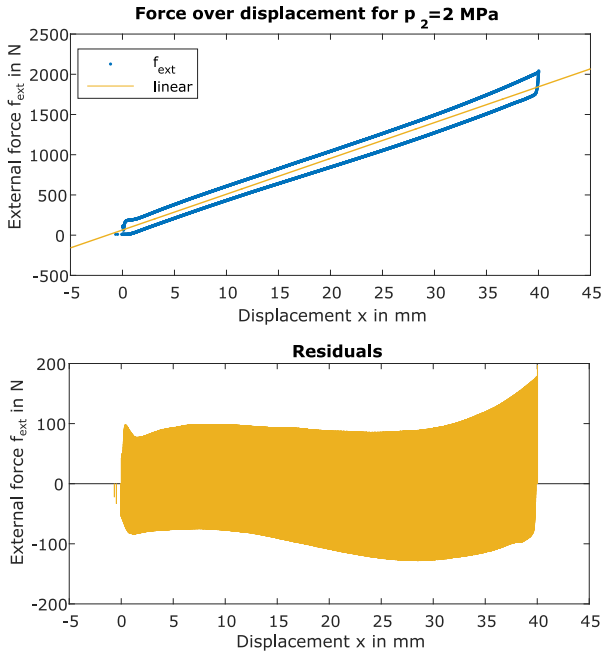

Fig. 11. Force–displacement plot for $p_2 = 2\,\text{MPa}$ in a low speed experiment to demonstrate the nearly linear spring behavior. Additional to the remaining nonlinearity, reasonable Coulomb friction can be observed in the residuals to the linear regression for this experiment.

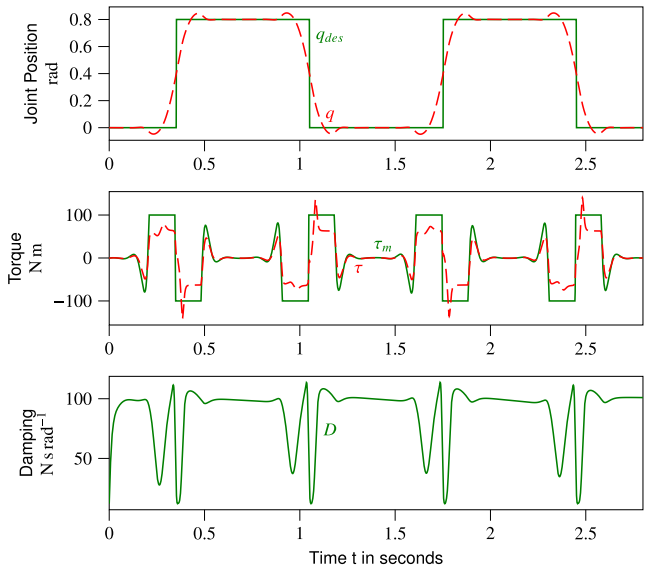

Fig. 12. Exemplary trajectory for the optimal control study, where $A = 0.8\,\text{rad}$, $T = 1.4\,\text{s}$ and the damping value can be varied from 12.1 to $200\,\text{N m s rad}^{-1}$.

collocation as well as all state and input constraints are taken into account in form of inequality constraints. All solutions were found using the interior point method IPOPT by [17]. Fig. 12 shows the plot of an exemplary trajectory.

5.0.2. Search space

In order to explore a representative set of possible application cases we sample the amplitude A in ten equidistant steps from $0.1\,\text{rad}$ to $1\,\text{rad}$. The period time T is sampled in 15 steps around the system's eigenfrequency $\omega = \frac{1}{2\pi}\sqrt{\frac{K}{M}} \approx 3.03\,\text{Hz}$, i.e., $T \in \{0.2\,\text{s}, 0.3\,\text{s}, \dots, 1.6\,\text{s}\}$. Four actuator settings for K and D where chosen to compare: one parameter set representing the VVEA system presented here, a set representing the ideal VVEA system (iVVEA), the SEA case and a case representing a LWR joint. The parameters are collected in Table 4.

Table 4
Actuator setting parameters.

	K N m rad^{-1}	D_{min} N m s rad^{-1}	D_{max} N m s rad^{-1}
VVEA	362	12.1	200
iVVEA	362	0	200
SEA	362	0	0
LWR	30 000	30 000	30 000

5.0.3. Results

Fig. 13 shows the optimal control results for all cases over T and A. White points mark cases where no setup can deliver a valid trajectory where the amplitude of the link reaches up to 95% of the desired amplitude A (i.e. less than 5% tracking error normalized to A). In blue marked cases SEA archives the least error, turquoise points mark cases where the LWR setup is best and in purple cases the proposed VVEA performs best.

In direct comparison our presented VVEA archives in 29.1% of analyzed cases better tracking performance than a SEA with the same stiffness. The ratio of the mean RMSE of the SEA (LWR) over the mean RMSE of the VVEA's is 0.934 (1.104). Only small amplitudes can be tracked by LWR setup best.

The iVVEA gets in 89.6% of analyzed cases a better tracking performance than a SEA with the same stiffness. As the SEA setup is contained in an iVVEA varying from 0 to $200\,\text{N m s rad}^{-1}$. Thus, this rate must be caused by suboptimal numerical solutions of the optimal control

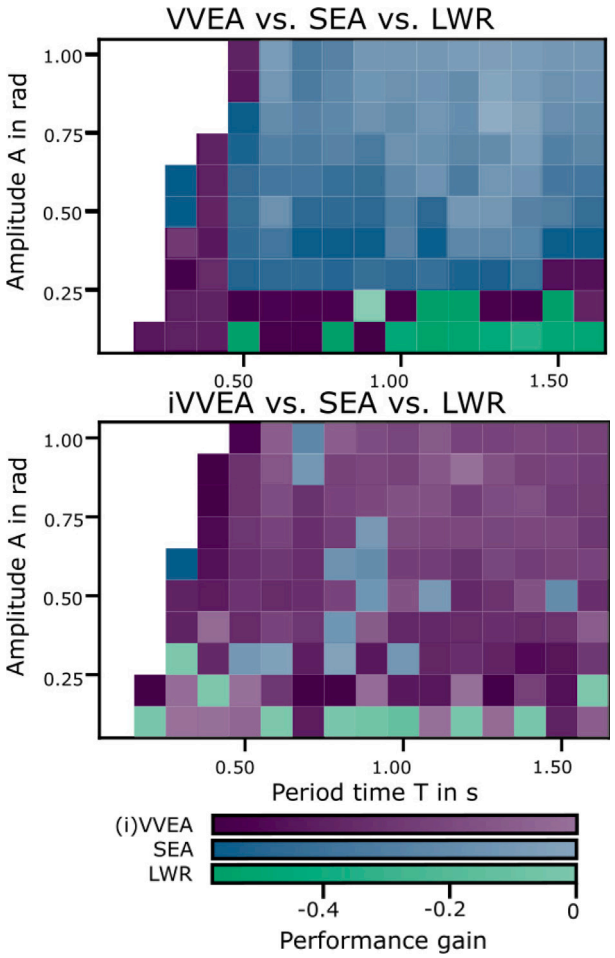

Fig. 13. Distribution of the best performing setup over application scenarios. Blue depicts cases in which the SEA performs the best. Turquoise indicates the LWR actuator and purple stands for the VVEA. Non valid trajectories are marked white. Deeper colors mark samples with bigger performance gain compared to the next best solution. The upper figure shows the damping range of our presented hardware, i.e., $12.1 \leq D \leq 200\,\mathrm{N\,m\,s\,rad^{-1}}$. The lower plot shows the ideal case with $0 \leq D \leq 200\,\mathrm{N\,m\,s\,rad^{-1}}$.

problem, i.e., the solver found only local minima in those cases. The ratio of the mean RMSE of the SEA over the mean RMSE of the iVVEA's is 1.243. An iVVEA can outperform the LWR setup in 90.8% of the cases. The ratio of the mean RMSE of the LWR over the mean RMSE of the iVVEA's is 1.521. Only small amplitudes can be tracked by LWR setup best. Table 5 sums the results up.

Remark 3. It is worth remarking that for robots featuring VVEAs, static state feedback can achieve at most input–output linearization and decoupling, since an internal nonlinear dynamics is left in the closed-loop system. Consequently, control designs based on static feedback becomes ill-conditioned as joint viscosity decreases. These critical aspects are discussed in detail in [18]. In scenarios that require the deactivation (or strong variation) of the physical damper, one must therefore resort to dynamic state feedback, such as proposed by the impedance controller in [19]. This controller has been successfully evaluated on the predecessor of the proposed VVEA.

6. Balancing performance and safety

As shown in [12] increased physical damping enhances the performance of the actuator while compromising the safety. Hence, for safety reasons, the goal for a physical damping setpoint policy should be: "Set the damping as low as possible". On the contrary, the best performance and efficiency is achieved with the highest possible physical damping set.

Table 5
Summary of the achieved performance for VVEA compared to LWR and SEA joints.

29.1%	89.2%	of cases VVEA outperforms SEA/LWR
89.6%	90.8%	of cases iVVEA outperforms SEA/LWR
0.934	1.10	RMS of SEA/LWR over RMS of VVEA
1.24	1.52	RMS of SEA/LWR over RMS of iVVEA

Table 6
Optimal control problem parameters.

P_τ	$4 \times 10^4\ 1/\mathrm{N^2 m^2}$
P_d	$2.5 \times 10^{-2}\ \mathrm{s^2\,N^{-2}\,m^2}$
P_m	$1 \times 10^1\ 1/\mathrm{N^2 m^2}$
t_e	0.5 s

To analyze the safety potential of an online variable damping setpoint we compare three cases in an optimal torque control study utilizing the same optimization framework from above. The optimization problem was formulated as

$$\min_{\tau_m, u_d} \int_0^{t_e} P_\tau(\tau - \tau_{\mathrm{ref}})^2 + P_d(D - D_{min})^2 + P_m \tau_m^2 dt$$

subject to the system dynamic Eqs. (8), (9) and (10) as well as the constraints on motor torque and damper variability given by (13),(11) and (12). To accelerate simulation time we set the friction $C_f = 0$. The parameters were chosen as in Table 6. The main control goal was to achieve torque tracking. Therefore, we selected a high value for the coefficient P_τ, which enforces that τ is close to τ_{ref}. To incorporate the trade-off between safety and torque tracking P_d ensures that D is chosen close to its minimum, if possible. Motor torques are reduced by having some small cost scaled with P_m. In this study, the link inertia was set to $M = 1{\times}10^4\,\mathrm{kg\,m^2}$ to simulate an almost fixed output scenario. See Fig. 14 for a comparison of the optimal trajectory for case (a): varying τ_m and u_d, case (b): fixed $D = 31\,\mathrm{N\,m\,s\,rad^{-1}}$ and case (c): fixed $D = 200\,\mathrm{N\,m\,s\,rad^{-1}}$ to represent a high damped case.

Fig. 14 shows that the performance loss in the torque tracking of the varying damping case (a) is small compared to the high damped case (c). In the varying damping case (a) (green) the actual torque reaches the desired torque nearly as fast as in case (c) (blue), while case (b) (red) is significantly slower. With regard to safety, case (a) and (b) share the same mean damping value $D = 31\,\mathrm{N\,m\,s\,rad^{-1}}$ and thereby exhibit similar safety behavior during unforeseen collisions. The third plot of Fig. 14 shows the trajectory of the damping value. It converges to the allowed minimum of $D = 12.1\,\mathrm{N\,m\,s\,rad^{-1}}$ around $t = 0.4$ s when the motor finally has loaded the spring to τ_{ref}.

7. Conclusion

In this paper we presented the mechanical design of a pull type spring–damper system. We could show that a linearity derivation below 2% is possible for a pneumatic spring. Within experiments we could confirm this behavior and obtain a total deviation including friction of less than 10%. An online variable damping allows adaption of the system over a wide range. Identified parameters for a simple dynamic model of the system allow estimation of the generated forces with an error less than 12%. Online variation of the damping parameter can improve torque tracking performance without compromising impact safety. Position tracking performance for repetitive point to point motions can be improved by up to 150% utilizing the variability of the damping coefficient.

A reduction of the minimal settable damping efficient can considerably improve the point to point tracking behavior.

Further refinements on the damping valve are necessary for next iterations to relax positioning requirements for higher damping setpoints.

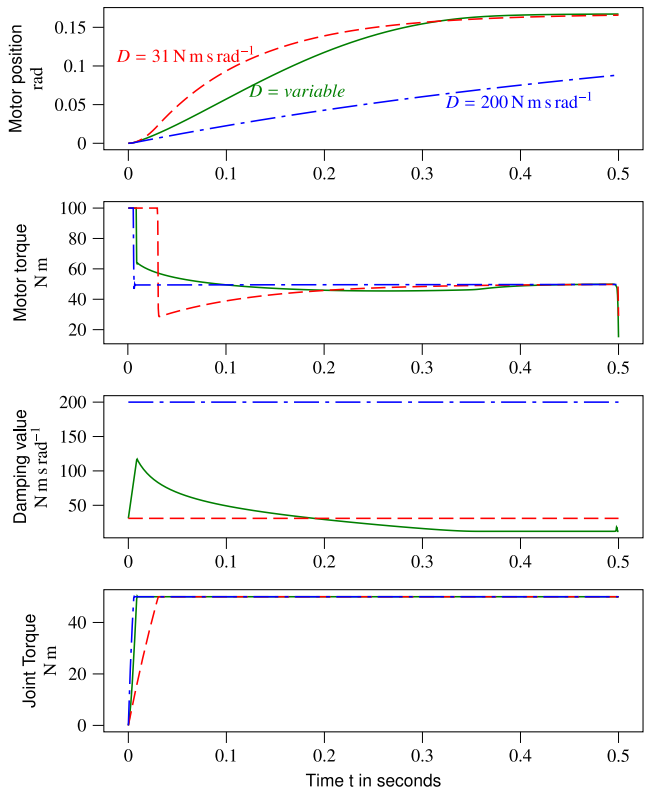

Fig. 14. Optimal trajectories for a 50 N m torque step. Simulation results for three damping strategies: optimized variable damping (green), high fixed damping (blue) and fixed damping near the mean of the variable case (red).

CRediT authorship contribution statement

Florian C. Loeffl: Writing – review & editing, Writing – original draft, Methodology, Investigation, Conceptualization, Resources, Software, Visualization. **Fabian Beck:** Writing – review & editing, Methodology, Investigation, Software, Visualization. **Jinoh Lee:** Writing – review & editing. **MinJun Kim:** Writing – review & editing. **Manuel Keppler:** Writing – review & editing, Conceptualization, Writing – original draft.

Declaration of competing interest

The authors declare that they have no known competing financial interests or personal relationships that could have appeared to influence the work reported in this paper.

Acknowledgments

This project has received funding from the European Research Council (ERC) under the European Union's Horizon 2020 research and innovation program with the grant agreement No 819358, NatDyReL.

Data availability

Data will be made available on request.

References

[1] Pratt GA, Williamson MM. Series elastic actuators. In: Intelligent robots and systems 95. 'Human robot interaction and cooperative robots', proceedings. IEEE/RSJ international conference on, volume 1. IEEE; 1995, p. 399–406.
[2] Kemper K, Koepl D, Hurst J. Optimal passive dynamics for torque/force control. In: 2010 IEEE international conference on robotics and automation. 2010, p. 2149–54.
[3] Enoch A, Sutas A, Nakaoka S, Vijayakumar S. Blue: A bipedal robot with variable stiffness and damping. In: Humanoid robots (humanoids), 2012 12th IEEE-RAS international conference on. IEEE; 2012, p. 487–94.
[4] Catalano MG, Grioli G, Garabini M, Belo FAW, Di Basco A, Tsagarakis NG, Bicchi A. A variable damping module for variable impedance actuation. In: ICRA. 2012, p. 2666–72.
[5] Accoto D, Tagliamonte N, Carpino G, Sergi F, Palo M, Guglielmelli E. pvej: A modular passive viscoelastic joint for assistive wearable robots. In: Proceedings - IEEE international conference on robotics and automation. 2012, p. 3361–6.
[6] Laffranchi M, Chen L, Kashiri N, Lee J, Tsagarakis NG, Caldwell DG. Development and control of a series elastic actuator equipped with a semi active friction damper for human friendly robots. Robot Auton Syst 2014;62:1827–36.
[7] Zhi D, Feng Z, Xu W, Kang R, Chen L. Design and control of a variable viscous damping actuator (VVDA) for compliant robotic joints. In: 2018 IEEE international conference on robotics and biomimetics. ROBIO, 2018, p. 1876–81.
[8] Yin C, Zhai X, Sun X, Wang S, Wong PK. Design and performance research of a hydro-pneumatic suspension with variable damping and stiffness characteristics. J Mech Sci Technol 2022;36:4913–23.
[9] Yuan P, Liu J, Branson DT, Song Z, Wu S, Dai JS, Kang R. Design and control of a compliant robotic actuator with parallel spring-damping transmission. Robotica 2024;42:1113–33.
[10] Monteleone S, Negrello F, Catalano MG, Garabini M, Grioli G. Damping in compliant actuation: A review. IEEE Robot Autom Mag 2022;2–21.
[11] Kumar JS, Paul PS, Raghunathan G, Alex DG. A review of challenges and solutions in the preparation and use of magnetorheological fluids. Int J Mech Mater Eng 2019;14:1–18.
[12] Laffranchi M, Chen L, Tsagarakis NG, Caldwell DG. The role of physical damping in compliant actuation systems. In: 2012 IEEE/RSJ international conference on intelligent robots and systems. 2012, p. 3079–85, ISSN: 2153-0866.
[13] Boyle R. A defence of the doctrine touching the spring and weight of the air propos'd by Mr. R. Boyle in his new physico-mechanical experiments, against the objections of Franciscus Linus; wherewith the objector's funicular hypothesis is also examin'd, by the author of those experiments. 1682.
[14] Loeffl F, Werner A, Lakatos D, Reinecke J, Wolf S, Burger R, Gumpert T, Schmidt F, Ott C, Grebenstein M, et al. The dlr c-runner: Concept, design and experiments. In: Humanoid robots (humanoids), 2016 IEEE-RAS 16th international conference on. IEEE; 2016, p. 758–65.
[15] Hirzinger G, Sporer N, Albu-Schaffer A, Hahnle M, Krenn R, Pascucci A, Schedl M. Dlr's torque-controlled light weight robot iii-are we reaching the technological limits now? In: Proceedings 2002 IEEE international conference on robotics and automation (cat. no. 02CH37292), vol. 2. 2002, p. 1710–6, vol.2.
[16] Andersson JAE, Gillis J, Horn G, Rawlings JB, Diehl M. CasADi – A software framework for nonlinear optimization and optimal control. Math Program Comput 2019;11:1–36.
[17] Wächter A, Biegler LT. On the implementation of an interior-point filter line-search algorithm for large-scale nonlinear programming. Math Program 2006;106:25–57.
[18] De Luca A, Farina R, Lucibello P. On the control of robots with visco-elastic joints. In: Proceedings of the 2005 IEEE international conference on robotics and automation. IEEE; 2005, p. 4297–302.
[19] Keppler M, Lakatos D, Werner A, Loeffl F, Ott C, Albu-Schäffer A. Visco-elastic structure preserving impedance (vesπ) control for compliantly actuated robots. In: 2018 European control conference. ECC, 2018, p. 255–60.